Journal of the Mechanics and Physics of Solids 61 (2013) 219–234

Contents lists available at SciVerse ScienceDirect

Journal of the Mechanics and Physics of Solids

journal homepage: www.elsevier.com/locate/jmps

Shear band in sand with spatially varying density

Ronaldo I. Borja [a,*], Xiaoyu Song [a], Amy L. Rechenmacher [b], Sara Abedi [c], Wei Wu [d]

[a] Department of Civil and Environmental Engineering, Stanford University, Stanford, CA 94305-4020, USA
[b] Department of Civil and Environmental Engineering, University of Southern California, Los Angeles, CA 90089-2531, USA
[c] Department of Civil and Environmental Engineering, Massachusetts Institute of Technology, Cambridge, MA 02139-4307, USA
[d] Institut für Geotechnik, Universität für Bodenkultur, Feistmantelstraße 4, 1180 Vienna, Austria

ARTICLE INFO

Article history:
Received 9 July 2011
Received in revised form
24 July 2012
Accepted 25 July 2012
Available online 7 August 2012

Keywords:
Bifurcation
Digital Image Correlation
Heterogeneous sand
Shear band
Strain localization

ABSTRACT

Bifurcation theory is often used to investigate the inception of a shear band in a homogeneously deforming body. The theory predicts conjugate shear bands that have the same likelihood of triggering. For structures loaded symmetrically the choice of which of the two conjugate shear bands will persist is arbitrary. In this paper we show that spatial density variation could be a determining factor for the selection of the persistent shear band in a symmetrically loaded localizing sand body. We combine experimental imaging on rectangular sand specimens loaded in plane strain compression with mesoscale finite element modeling on symmetrically loaded sand specimens to show that spatial heterogeneity in density does have a profound impact on the persistent shear band.

1. Introduction

Strain localization is a ubiquitous feature of granular materials undergoing nonhomogeneous deformation. In soils and rocks, the zone of localized deformation is generally referred to either as a shear band, fault, rupture zone, or simply a failure plane. The formation and evolution of these zones are commonly explained by either fracture mechanics (Horii and Nemat-Nasser, 1985; Ashby and Hallam, 1986) or bifurcation theory (Rice and Rudnicki, 1980; Rudnicki and Rice, 1975). Regardless of the material venue, be it powdered metals, porous rock, or soil, one consistent observation is that localized deformation is followed by a reduction in the overall strength as loading proceeds (Read and Hegemier, 1984; Viggiani et al., 1994; Kolymbas, 2009; Tejchman et al., 2007; Borja and Andrade, 2006).

In a homogeneously deforming body, bifurcation theory identifies conjugate shear bands but not the specific band that will eventually persist. The point of initiation of localized deformation and the selection of which shear band to propagate are often dictated by the location and direction of loading, the geometric configuration of the structure, and the boundary conditions. For example, a failure surface under a footing subjected to an inclined load should position and orient according to the location and inclination of the load. However, when a footing is loaded symmetrically an ambiguity arises as to which of the two conjugate directions the failure surface will eventually trace. Because geomaterials such as soils and rocks are far from being homogeneous, there is a compelling argument that spatial heterogeneity in the void ratio distribution may have a profound impact on the final orientation of the persistent shear band in symmetrically loaded sand bodies. To investigate the role of spatial variation in density on the localization of deformation in symmetrically loaded sand bodies, we pursue a combined experimental–numerical modeling program in which the spatial variation of

* Corresponding author.
E-mail address: borja@stanford.edu (R.I. Borja).

0022-5096/$ - see front matter © 2012 Elsevier Ltd. All rights reserved.
http://dx.doi.org/10.1016/j.jmps.2012.07.008

density is quantified by X-ray Computed Tomography (CT) imaging and input into a finite element (FE) model that then predicts the constitutive response of the sand body according to this quantified density. The predicted response is then validated against digital image-based displacement maps derived from the experiments.

There has been an extensive body of literature documenting cases of strain localization in the laboratory, and how the important signatures of localized deformation have been measured and quantified. Experimental capture of the bifurcation process in soils is challenged in that testing within a sealed membrane and cell or amidst opaque confining plates hampers the ability to "visualize" internal specimen deformations. When relying on boundary measurements, the exact nature of localization is difficult to capture in that a shear band typically becomes visible only after it has completely propagated through the specimen and created an offset across the specimen membrane (Shapiro and Yamamuro, 2003). In spite of these challenges, a variety of experimental investigations have been undertaken.

One category of approaches has focused on measuring physical grain-level displacements in the vicinity of the shear band. Local displacements and strains and shear band geometry have been measured from displacements of embedded markers (Stroud, 1971), grid points painted on the specimen membrane (Desrues, 1984; Yoshida et al., 1994; Liang et al., 1997; Alshibli and Sture, 2000), and by photographically tracking individual sand grain motion (Harris et al., 1995; Mooney et al., 1996, 1998). With these techniques, however, only an average sense of behavior is obtained.

Experimental methods aimed at quantifying spatial density variations have been employed to improve displacement measurement of grid points (see, e.g. Liang et al., 1997; Alshibli and Sture, 2000). The main techniques used have been gamma-ray (Coumoulos, 1968; Desrues et al., 1985) and X-ray CT (Desrues et al., 1996; Alshibli et al., 2000; Alshibli and Hasan, 2008). These techniques derive quantitative measurements of local density through correlation with measured radiation attenuations. The CT technique in particular is very effective at delineating subtle material density variations, such as the lower density sand material within a shear band, and as such has enabled precise quantifications of shear band patterning, inclination and thickness. Due to the nature of the required radiation sources, however, the specimen cannot be analyzed within the confines of traditional test cells. Thus, work to date has been limited to specimens held only under vacuum confinement, analyses over wide strain increments, and/or analysis of only one failed state. More recently, the technique of micro-Computed Tomography (μ-CT) has enabled very precise detection of individual sand grains, providing detailed particle position and contact maps and calculations of local void ratios (Hasan and Alshibli, 2010; Tagliaferri et al., 2011). However, the technique is currently limited to only very small specimens: currently only cm-sized specimens (Tagliaferri et al., 2011) or cm-sized cores taken from inside of larger, epoxy-hardened specimens (Hasan and Alshibli, 2010) have been analyzed. Moreover, the CT method in general does not yield kinematic data, in particular over the relatively small strain increments over which shear bands form; thus, the location and thickness of the shear band is merely inferred from variations in microstructure or density data.

Quantitative analyses of local void ratio also have been accomplished using microscopic images of very thin slices of sand material prepared from epoxy-hardened specimens (Oda and Kazama, 1998; Alshibli and Sture, 1999; Jang and Frost, 2000; Evans and Frost, 2010). Void ratios are calculated based on the relative areas occupied by voids and solids. While this approach allows thorough examination of shear band microstructure, void ratio is computed only over a portion of the shear band. However, as kinematic data is not availed, shear band location has to be inferred solely from particle positions. Also, the destructive and forensic nature of the technique inhibits the exploration of temporal evolution. Matsushima et al. (2002) used Laser-Aided Tomography (LAT) to observe, through laser illumination, grain motions in the interior of plane strain specimens. However, the nature of the technique requires use of fully transparent particles (e.g. crushed glass), and thus currently does not permit behavioral analysis of real soils.

The technique of Digital Image Correlation (DIC) was used to directly quantify local displacements on the surfaces of sand specimens throughout plane strain compression (Rechenmacher et al., 2010, 2011; Rechenmacher and Finno, 2004; Rechenmacher, 2006; Chupin et al., 2011). The DIC technique operates by matching pixel patterns between high resolution digital images. The displacement information has been used to quantify volumetric evolutions to critical state in dilative sands, measure thickness and inclination of persistent shear bands, and investigate the uniformity of strains along a persistent shear band. DIC has shown great promise toward enabling quantitative, nondestructive capture of the meso-scale kinematics associated with shear band formation (Rechenmacher, 2006), in particular in the presence of material heterogeneity.

There has been much progress in the literature pertaining to the development of constitutive models for strain localization analysis in sands, with particular emphasis on the impact of spatial density variation on the ensuing shear band. A key aspect of the modeling effort is the "mesoscale" level of material characterization. As a matter of terminology, the term "mesoscale" refers to a scale larger than the grain scale (microscale) but smaller than the element, or specimen, scale (macroscale). Specimen response then is modeled and analyzed as a boundary-value problem, taking into consideration the spatial variation of some physically measurable mesoscale quantity or quantities affecting the local soil response, such as density. It must be noted that the soil density has been known for a long time to correlate well with soil stiffness (Poulos, 1975; Vesic, 1975; Kulhawy and Mayne, 1990; Holtz, 1991), and thus any measured local density variation reflects the spatial variation in the local soil stiffness. The success of the mesoscale approach in studying strain localization in soils relies on the advances in the experimental measurement of the initial, spatial, mesoscale parameter variation in the specimen (using CT) as well as the specimen deformation fields before and after localization (using DIC).

A constitutive model for sand that uses the density, or void ratio, as a principal state variable is the so-called 'Nor-Sand' critical state model developed by Jefferies (1993). This model contains a state variable ψ_i that effectively 'detaches' the void ratio from the critical state line. In conventional critical-state formulations based on Cam-Clay plasticity (Roscoe and

Burland, 1969; Borja and Lee, 1990; Borja, 1991), prescribing the critical state line and the current state of stress uniquely determines the void ratio, so the current state of stress and the current density cannot be prescribed independently. The Nor-Sand formulation relaxes this restriction through the state variable ψ_i in the sense that for the same critical state line and current state of stress a spatial variation of density can be prescribed separately. The formulation by Jefferies, however, is not complete in that it lacks an elastic component. Furthermore, it cannot accommodate for the effect of the third stress invariant and a nonassociative plastic flow that may be critical for strain localization simulation. Relatively recent work (Borja and Andrade, 2006; Andrade and Borja, 2006) thus reformulated the Jefferies model to provide the missing ingredients of the constitutive theory. This reformulated constitutive model forms the basis of the present work.

2. Theoretical development

We restrict the theory to the usual quasi-static problem focused on the initiation of a shear band in a heterogeneous body. We state the governing equations of equilibrium to impose, as well as the constitutive assumptions on the material.

2.1. Momentum balance and localization condition

Our point of departure is the weak form of the linear momentum balance in a body $\mathcal{B}$ bounded by surface $\partial\mathcal{B}$ reckoned with respect to the reference configuration (Borja, 2002)

$$\mathcal{J}(\phi,\boldsymbol{\eta}) = \int_{\mathcal{B}} (\mathrm{GRAD}\,\boldsymbol{\eta} : \boldsymbol{P} - \rho_0 \boldsymbol{\eta}\cdot\boldsymbol{G})\,\mathrm{d}V - \int_{\partial\mathcal{B}^t} \boldsymbol{\eta}\cdot\boldsymbol{t}\,\mathrm{d}A, \tag{1}$$

where $\boldsymbol{P}$ is the nonsymmetric first Piola–Kirchhoff stress tensor, ϕ is the motion with an associated variation $\boldsymbol{\eta}$, ρ_0 is the mass density in the reference configuration, $\boldsymbol{G}$ is the gravity acceleration vector, $\boldsymbol{t}$ is the nominal traction vector, and GRAD is the gradient operator with respect to the reference configuration. The surface $\partial\mathcal{B}$ admits the decomposition $\partial\mathcal{B} = \partial\mathcal{B}^t \cup \partial\mathcal{B}^\phi$ and $\emptyset = \partial\mathcal{B}^t \cap \partial\mathcal{B}^\phi$, where $\partial\mathcal{B}^\phi$ and $\partial\mathcal{B}^t$ are the Dirichlet and Neumann boundaries, respectively, and the overline denotes a closure. Balance of momentum then yields $\mathcal{J}(\phi,\boldsymbol{\eta}) = 0$ in the weak sense. We note that shear band development is sensitive to the evolving geometrical configuration, so a finite deformation formulation is employed in this work.

In the presence of a shear band defined by surface $\mathcal{S}$ in the interior of $\mathcal{B}$, the discontinuity on $\mathcal{S}$ can be eliminated from the first term of $\mathcal{J}$ by writing

$$\int_{\mathcal{B}\setminus\mathcal{S}} \mathrm{GRAD}\,\boldsymbol{\eta} : \boldsymbol{P}\,\mathrm{d}V = -\int_{\mathcal{B}\setminus\mathcal{S}} \boldsymbol{\eta}\cdot\mathrm{DIV}\,\boldsymbol{P}\,\mathrm{d}V + \int_{\mathcal{S}} \boldsymbol{\eta}\cdot(\llbracket \boldsymbol{P}\cdot\boldsymbol{N}\rrbracket)\,\mathrm{d}A + \int_{\partial\mathcal{B}^t} \boldsymbol{\eta}\cdot(\boldsymbol{P}\cdot\boldsymbol{v})\,\mathrm{d}A, \tag{2}$$

where $\boldsymbol{N}$ is the unit normal vector to $\mathcal{S}$ in the reference configuration, $\boldsymbol{v}$ is the unit normal vector to $\partial\mathcal{B}$, and $\llbracket \boldsymbol{P}\cdot\boldsymbol{N}\rrbracket$ is a possible jump in the nominal traction vector on $\mathcal{S}$. Inserting into (1), setting $\mathcal{J} = 0$, and using standard argument yields the equivalent strong form

$$\mathrm{DIV}\,\boldsymbol{P} + \rho_0\boldsymbol{G} = \boldsymbol{0} \quad \text{in } \mathcal{B}\setminus\mathcal{S}, \tag{3}$$

$$\boldsymbol{P}\cdot\boldsymbol{v} = \boldsymbol{t} \quad \text{on } \partial\mathcal{B}^t, \tag{4}$$

subject to the jump condition

$$\llbracket \boldsymbol{P}\cdot\boldsymbol{N}\rrbracket = \llbracket \boldsymbol{P}\rrbracket\cdot\boldsymbol{N} = \boldsymbol{0} \quad \text{on } \mathcal{S}, \tag{5}$$

where DIV is the divergence operator in the reference configuration. We see that the jump condition on the shear band makes use of the nominal traction vector $\boldsymbol{t}$.

Tangent stiffness tensors are needed to enforce the localization condition. To this end, we write the variation of $\mathcal{J}$ as

$$\delta\mathcal{J} = \int_{\mathcal{B}} \mathrm{GRAD}\,\boldsymbol{\eta} : \mathbf{A} : \delta\boldsymbol{F}\,\mathrm{d}V - \int_{\partial\mathcal{B}^t} \boldsymbol{\eta}\cdot\delta\boldsymbol{t}\,\mathrm{d}A, \tag{6}$$

where "δ" denotes variation, $\boldsymbol{F}$ is the deformation gradient, and $\mathbf{A}$ is a two-point tangent stiffness tensor defined by the relation

$$\delta\boldsymbol{P} = \mathbf{A} : \delta\boldsymbol{F}, \quad \mathbf{A} = \frac{\partial\boldsymbol{P}}{\partial\boldsymbol{F}}, \quad \mathsf{A}_{iAjB} = \frac{\partial P_{iA}}{\partial F_{jB}}. \tag{7}$$

In terms of the variations, the strong form with dead loading reads

$$\mathrm{DIV}\,\mathbf{A} : \delta\boldsymbol{F} = \boldsymbol{0} \quad \text{in } \mathcal{B}\setminus\mathcal{S}, \tag{8}$$

$$(\mathbf{A} : \delta\boldsymbol{F})\cdot\boldsymbol{v} = \delta\boldsymbol{t} \quad \text{on } \partial\mathcal{B}^t, \tag{9}$$

subject to the condition

$$\llbracket \mathbf{A} : \delta\boldsymbol{F}\rrbracket\cdot\boldsymbol{N} = \boldsymbol{0} \quad \text{on } \mathcal{S}. \tag{10}$$

If the tangent operator $\mathbf{A}$ is continuous across the band, the localization condition (10) can be written in a more specialized form $(\mathbf{A} : [\![\delta \boldsymbol{F}]\!]) \cdot \boldsymbol{N} = \mathbf{0}$, where $[\![\delta \boldsymbol{F}]\!] = [\![\boldsymbol{V}]\!] \otimes \boldsymbol{N}/h_0$ and $[\![\boldsymbol{V}]\!]$ is the velocity jump; and h_0 is the band thickness in the reference configuration. In the context of elasto-plasticity, this condition is called continuous (or loading–loading) bifurcation (Borja, 2002), with plastic loading assumed to take place inside and outside the band during bifurcation. The jump condition is then

$$\frac{1}{h_0} \boldsymbol{A} \cdot [\![\boldsymbol{V}]\!] = \mathbf{0}, \quad A_{ij} = N_A \mathsf{A}_{iAjB} N_B. \tag{11}$$

Nontrivial solutions are possible when $\det(\boldsymbol{A}) = 0$ for some critical band orientation $\boldsymbol{N}$ measured with respect to the reference configuration. Equivalently, the localization condition can be written as

$$\frac{h_0}{h^2} \boldsymbol{a} \cdot [\![\boldsymbol{v}]\!] = \mathbf{0}, \quad a_{ij} = n_k (F_{kA} A_{iAjB} F_{lB}) n_l, \tag{12}$$

where h is the band thickness in the current configuration. Nontrivial solutions are then possible when $\det(\boldsymbol{a}) = 0$ for some critical band orientation $\boldsymbol{n}$ in the current configuration. The eigenvectors $[\![\boldsymbol{V}]\!]$ and $[\![\boldsymbol{v}]\!]$ are the same when normalized with respect to their magnitude since they reflect the same jump in velocity at the moment of bifurcation (see Borja, 2002 for further details of the theory).

2.2. Constitutive assumptions

A constitutive model is necessary to define the evolution of $\boldsymbol{P}$ with $\boldsymbol{F}$, and here we use multiplicative plasticity theory along with a critical state model to represent the behavior of sand. Because $\boldsymbol{P}$ is a two-point tensor (force in the current configuration per unit area in the reference configuration), it is not a convenient stress measure to use for constitutive modeling. A more natural stress measure is the one-point symmetric Kirchhoff stress tensor $\boldsymbol{\tau} = \boldsymbol{P} \cdot \boldsymbol{F}^{\mathrm{T}}$ (force and areas are defined in the same current configuration), which is related to the Cauchy stress tensor $\boldsymbol{\sigma}$ via $\boldsymbol{\tau} = J\boldsymbol{\sigma}$, where $J = \det(\boldsymbol{F})$ is the Jacobian of the motion. For the deformation measure we select the elastic left Cauchy–Green deformation tensor $\boldsymbol{b}^{\mathrm{e}}$ to pair with the stress tensor $\boldsymbol{\tau}$ in a hyperelastic constitutive formulation. Isotropy in the elastic response implies that the two tensors are co-axial.

The proposed constitutive model for sand has been reported before (Borja and Andrade, 2006; Andrade and Borja, 2006), and here we simply summarize the main features of this model. The intent is to elucidate the model parameters inasmuch as a main challenge of the proposed work is to determine these parameters. The model adopts a hyperelastic–plastic split in the elastic logarithmic principal stretches. On the assumption of co-axiality this means that we only need to deal with the principal values of the stresses and strains. The hyperelastic part can capture pressure-dependent elastic bulk and shear moduli. Laboratory experiments relevant for obtaining the hyperelastic model parameters are described in Borja et al. (1997).

For the plasticity part we use a (p,q,θ) representation analogous to the cylindrical Haigh–Westergaard coordinates (Chen and Han, 1988; Sfriso and Weber, 2010), where the hydrostatic axis serves as the pole and any of the three positive principal axes of the Kirchhoff stress serves as the polar axis. The invariants are

$$p = \frac{1}{3} \operatorname{tr}(\boldsymbol{\tau}), \quad q = \sqrt{\frac{3}{2}} \|\boldsymbol{s}\|, \tag{13}$$

where $\boldsymbol{s} = \operatorname{dev}(\boldsymbol{\tau})$, and $\theta \in [0, \pi/3]$ is Lode's angle determined from the equation

$$\cos 3\theta = \sqrt{6} \frac{\operatorname{tr}(\boldsymbol{s}^3)}{[\operatorname{tr}(\boldsymbol{s}^2)]^{3/2}}. \tag{14}$$

The ellipticity is

$$\rho = \|\boldsymbol{s}\|_{\mathrm{ext}} / \|\boldsymbol{s}\|_{\mathrm{com}}, \quad 1/2 \le \rho \le 1, \tag{15}$$

where $\|\boldsymbol{s}\|_{\mathrm{com}}$ and $\|\boldsymbol{s}\|_{\mathrm{ext}}$ are the yield function radii on the compressive and extensional principal stress axes, respectively, describing the deviation from roundness of the yield surface on the deviatoric plane. See Borja et al. (2003) for an alternative representation of the third stress invariant.

The yield function takes the form

$$f = \zeta q + \eta p \le 0, \tag{16}$$

where $\zeta = \zeta(\rho,\theta)$ is the Gudehus (1973) and Argyris et al. (1974) scaling function given by

$$\zeta(\rho,\theta) = \frac{(1+\rho) + (1-\rho)\cos 3\theta}{2\rho}. \tag{17}$$

This function is convex for $7/9 \le \rho \le 1$ (Jiang and Pietruszczak, 1988). Note that there are other functions that provide a wider range of ellipticity while maintaining convexity (see e.g. Willam and Warnke, 1974), but the ellipticity limit $\rho = 7/9$ is usually sufficient to capture the effect of the third invariant on the yielding of sands.

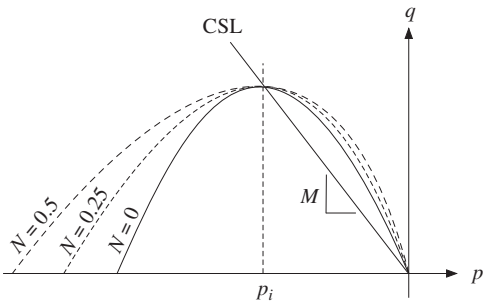

Fig. 1. Yield surfaces on (p,q)-plane. CSL, critical state line.

Eq. (16) contains the stress ratio η given by

$$\eta = \begin{cases} M[1+\ln(p_\mathrm{i}/p)] & \text{if } N=0, \\ (M/N)[1-(1-N)(p/p_\mathrm{i})^{N/(1-N)}] & \text{if } N>0, \end{cases} \tag{18}$$

where the parameter M is the slope of the critical state line (CSL) and has the same meaning as in the modified Cam-Clay model (Roscoe and Burland, 1969), and $p_\mathrm{i}<0$ is a plastic internal variable obtained by setting $f=0$,

$$\frac{p_\mathrm{i}}{p} = \begin{cases} \exp(\eta/M-1) & \text{if } N=0, \\ [(1-N)/(1-\eta N/M)]^{(1-N)/N} & \text{if } N>0. \end{cases} \tag{19}$$

The exponent parameter N determines the curvature of the yield surface on the hydrostatic axis, and typically has a value less than 0.4 for sands (Jefferies, 1993). Fig. 1 shows the geometric meaning of M, N, and p_i.

A plastic potential function of the following form captures nonassociative plastic flow:

$$g = \overline{\zeta} q + \overline{\eta} p, \tag{20}$$

where

$$\overline{\eta} = \begin{cases} M[1+\ln(\overline{p}_\mathrm{i}/p)] & \text{if } \overline{N}=0, \\ (M/\overline{N})[1-(1-\overline{N})(p/\overline{p}_\mathrm{i})^{\overline{N}/(1-\overline{N})}] & \text{if } \overline{N}>0. \end{cases} \tag{21}$$

The parameter $\overline{N}$ controls the amount of volumetric nonassociativity of the plastic flow, whereas $\overline{\zeta}=\overline{\zeta}(\overline{\rho},\theta)$ introduces nonassociativity with respect to the third invariant. The variable $\overline{p}_\mathrm{i}$ is a free parameter that can be chosen so that $g=0$ whenever $f=0$. Plastic flow then is associative if $\overline{N}=N$ and $\overline{p}_\mathrm{i}=p_\mathrm{i}$. Otherwise, the conditions

$$\overline{N} \le N \quad \text{and} \quad \overline{\zeta} \le \zeta, \tag{22}$$

must hold to ensure nonnegative plastic dissipation. These are met by choosing a dilatancy angle that is less than or at most equal to the friction angle at critical state (Andrade and Borja, 2006; Borja and Andrade, 2006). In this paper we shall consider an associative flow rule and take $\overline{N}=N$ and $\overline{\zeta}=\zeta$.

Plastic dilatancy is a key aspect of the constitutive model that makes it suitable for modeling strain localization. It is defined as

$$D = \dot{\epsilon}_v^\mathrm{p}/\dot{\epsilon}_s^\mathrm{p}, \tag{23}$$

where

$$\dot{\epsilon}_v^\mathrm{p} = \dot{\lambda}\,\mathrm{tr}\left(\frac{\partial g}{\partial \boldsymbol{\tau}}\right), \quad \dot{\epsilon}_s^\mathrm{p} = \dot{\lambda}\sqrt{\frac{2}{3}}\Omega, \quad \Omega = \left\|\mathrm{dev}\left(\frac{\partial g}{\partial \boldsymbol{\tau}}\right)\right\|. \tag{24}$$

Plastic dilatancy cannot be unbounded, and for sands there exists a maximum value D^* given by the expression

$$D^* = \alpha\psi_\mathrm{i}, \tag{25}$$

where ψ_i is a state variable describing the variation of the specific volume v independent of the mean normal stress, given by

$$\psi_\mathrm{i} = v - v_{c0} + \lambda\ln(-p_\mathrm{i}), \tag{26}$$

where v_{c0} is the reference specific volume. The parameter α is a negative number that was set to about -3.5 in previous work (Jefferies, 1993). We shall show in the present paper, however, that this parameter can be very important for a realistic capture of the persistent shear band in heterogeneous sands.

The hardening law has the form

$$\dot{p}_{\rm i} = h(p_{\rm i}^* - p_{\rm i})\dot{\epsilon}_s^{\rm p}, \tag{27}$$

where h is a dimensionless hardening parameter. The form of the hardening law differs from Cam-Clay-type models in that it uses the deviatoric plastic strain rate $\dot{\epsilon}_s^{\rm p}$ instead of the volumetric plastic strain rate $\dot{\epsilon}_v^{\rm p}$. In (27), $p_{\rm i}^*$ is an image pressure determined from

$$p_{\rm i}^* = p \times \begin{cases} \exp\left(\sqrt{\dfrac{2}{3}}\Omega\alpha\psi_{\rm i} \Big/ M\right) & \text{if } N = 0, \\ \left(1 - \sqrt{\dfrac{2}{3}}\Omega\alpha\psi_{\rm i} N \Big/ M\right)^{(N-1)/N} & \text{if } N > 0. \end{cases} \tag{28}$$

The parameters of the model are discussed further in the next section.

3. Experimental methods and procedures

The numerical predictions were validated against a plane strain compression test on a sand specimen imposed with a density imperfection. The specimen is 137 mm tall by 39.5 mm wide by 79.7 mm deep (out-of-plane). The specimen base rests on a low-friction, linear bearing sled, which permits the lateral offset required for unconstrained shear band propagation. The specimen out-of-plane faces are constrained by rigid, glass-lined, acrylic walls, which enforce the zero strain conditions as well as permit imaging of in plane specimen deformations. Load cells embedded between the glass and acrylic measure out-of-plane forces. All surfaces contacting the specimen are glass-lined and lubricated to minimize boundary friction. The apparatus has been described extensively elsewhere, see (Rechenmacher et al., 2010; Chupin et al., 2011).

The sand tested represents a 50–50% by mass sieved mixture of silica and concrete sands, herein called SC sand. The resulting sand is relatively uniform, with median grain diameter of 0.42 mm, coefficient of uniformity of 1.2, and specific gravity of 2.64. The reason for mixing two sands was to produce a color variation among sand grains to enable mapping by the DIC technique (described below). The specimen was prepared by dry pluviation with the density imperfection imposed as follows. Sand was rained initially from a constant drop height of 12 cm. When the specimen mold was about a quarter full, the drop height was abruptly lowered to 2 cm, and sustained at this height for another 3 cm of filling, after which it was abruptly returned back to 12 cm for the remainder of filling. The result was a dense sand specimen with about a 3-cm-thick layer of loose sand located at about the bottom third of the specimen height. The global dry density of the specimen was approximately 1.50 g/cm^3, or about 55% relative density. We estimate relative densities of the dense and loose zones to be about 65% and 15%, respectively. After preparation, the sand specimen was confined under 60 kPa vacuum pressure and transported to the USC Department of Radiology for scanning by X-ray Computed Tomography (CT).

In X-ray CT, the energy attenuation of an X-ray beam passing through a body is measured (e.g. Wellington and Vinegar, 1987). By collecting attenuation data from multiple directions, local energy attenuations internal to the body, which correlate with local material densities, can be back-calculated. Scans in multiple planes (slices) are pieced together to provide 3D density distributions through the entire body. CT scans in this research were performed on a Siemens Somatom Sensation 10 scanner, using an X-ray energy of 140 kV, radiation dose of 140 mAs, and 1 mm collimation (i.e., slice thickness). The voxel size (physical size of the volume element over which the attenuation coefficients are determined) was roughly 1 mm $\times$ 0.41 mm $\times$ 0.41 mm, which is sufficiently larger than a sand grain to enable detection of mesoscale material variation. CT attenuation data are referenced to an internationally standardized scale of dimensionless Hounsfield units, H. The Siemens scanner used in this research yields CT data in image format, with pixel values ranging between 0 (black) and 4095 (white), and these values can be considered as a linear shift from the H unit. For sands, the correlation between bulk sand dry density and H unit is linear (e.g. Desrues et al., 1996; Alshibli and Hasan, 2008). Such a linear correlation was developed for the SC sand and was used to obtain the specific volume measurements referenced below. After CT scanning, the specimen was transported back to the geomechanics laboratory, placed in the test cell, saturated, consolidated anisotropically to a mean normal effective stress of 130 kPa, and then sheared under displacement control.

At frequent intervals throughout testing (every 0.1% axial strain), digital images of in-plane specimen deformations were collected. A Q-Imaging PMI-4201 digital camera was used. DIC is a noninvasive technique that measures surface displacements on a deforming material by matching reference pixel subsets in an initial image state with target subsets in an image of the deformed state (e.g. Bruck et al., 1989; Sutton et al., 2000; Rechenmacher et al., 2010, 2011). Herein, this essentially translates to tracking the collective movement of clusters of sand grains. Subsets were overlapped, and center-to-center spacing was designed to achieve grain-scale resolution of displacement data. As will be seen below, the DIC analyses produced full field displacement maps, including the detailed capture of the onset and progression of strain localization. Displacement measurement accuracy is ± 0.009 mm. The software VIC-2D by Correlated Solutions, Inc. was used to conduct the DIC analyses.

4. Sensitivity analysis

The proposed constitutive model captures plastic dilatancy and localization of deformation in sands. Even though some of the material parameters can be determined from conventional laboratory tests, the model is of specialized nature. Thus, some of the material parameters must be inferred from inverse analysis whereas others may have to be assumed from previous work on similar sands. In what follows, we describe how we determined the values of the materials parameters used in the simulations. For clarity, the parameters have been classified into elastic and plastic groups, and their base values are shown in Tables 1 and 2, respectively.

Laboratory tests conducted on the SC sand included 1D loading and unloading tests on oedometer and drained plane strain compression tests with volume change measurement. The drained plane strain test on the (1,3)-plane involved increasing the vertical stress σ_1 while holding the in-plane horizontal stress σ_3 and pore water pressure u_w fixed. The out-of-plane normal stress σ_2 then varied during the loading phase. Test results included 1D compressibility void ratio-logarithm of pressure curves that have been converted into logarithmic specific volume-logarithmic vertical pressure based on the idea of a bilogarithmic compressibility law (Borja et al., 1997; Borja and Tamagnini 1998), and the time variations of the effective stresses σ'_1 and σ'_2 from the plane strain test. Because of the uncertainties in the measured values of the out-of-plane normal stress σ'_2, we only used the time variation of σ'_1 for inferring the values of the parameters.

The sand tested in the plane strain device had imposed density heterogeneity in it, so the mesoscopic response does not coincide with the specimen response for parameter calibration purposes. In order to determine the material parameters for the mesoscopic model, a key assumption must be made that the initial portion of the heterogeneous specimen's response may be taken to be about the same as that of the mesoscopic response. However, it is known that the response of a heterogeneous specimen during the late portion of loading may be significantly affected by the specimen heterogeneity, which enhances strain localization, so we only used the initial portion of the experimental stress-strain curve to infer the parameters for the mesoscopic model.

Given the limited number of tests conducted on the sand and the number of material parameters of the constitutive model, assumptions were made on the values of some of the parameters based on recommendations by previous authors and numerical tests conducted with the finite element model. In Table 1, the reference pressure p_0 and reference volumetric strain ϵ^e_{v0} simply establish the position of the hyperelastic curve, so the value of one parameter depends on the value of the other parameter. The parameter α_0 describes the pressure-dependence of the elastic shear modulus μ_0, but since the effective mean normal stress did not vary significantly during testing, we simply took a constant shear modulus from the initial slope of the σ'_1 versus ϵ_1 curve, and set α_0 equal to zero. The pressure-dependence of the elastic bulk modulus is defined by the value of the compressibility parameter κ determined from the unload–reload 1D compression tests.

Because the soil specimen experienced inhomogeneous deformation during testing, it would be more appropriate to treat it as a structure rather than an element for purposes of analysis. Thus, instead of reporting stress–strain responses we use a vertical load–vertical compression representation. The vertical load is the axial load responsible for shearing the specimen from its initial condition, and was measured directly from the test; if the plane strain specimen deformed uniformly and deformation was small, this would be equal to $(\sigma'_1-\sigma'_3)A$, where A is loading area of the specimen, but because deformation was large and nonuniform, the stresses cannot be inferred from this simple formula. The vertical compression, on the other hand, is simply the vertical shortening of the specimen.

Table 1
Parameters for the hyperelastic part of the constitutive model.

Parameter	Symbol	Value	From
Elastic compressibility index	κ	0.01	Test
Reference pressure	p_0	−112 kPa	Inferred
Reference volumetric strain	ϵ^e_{v0}	0	Assumed
Elastic shear modulus	μ_0	30 MPa	Inferred

Table 2
Parameters for the plastic part of the constitutive model.

Parameter	Symbol	Value	From
Slope of critical state line	M	1.2	Suggested[a]
Yield surface parameter	N	0.4	Suggested[a]
Ellipticity	ρ	7/9	Inferred
Hardening parameter	h	280	Inferred
Plastic compressibility index	λ	0.03	Test
CSL reference specific volume	v_{c0}	1.95	Estimated
Limit dilatancy parameter	α	−1.5	Inferred

[a] Values obtained from Jefferies (1993) for sands with similar gradation.

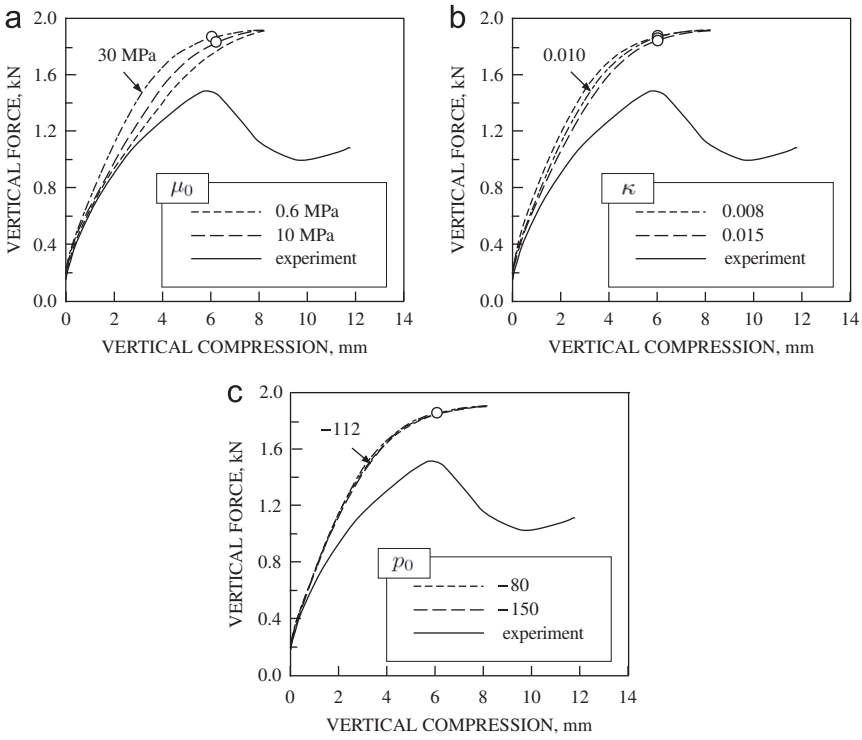

Fig. 2. Sensitivity of vertical force–vertical compression curve to variation of hyperelastic parameters: (a) shear modulus μ_0; (b) compressibility parameter κ; and (c) reference pressure p_0. Open dots denote shear-band bifurcation points. Only the shear modulus μ_0 has noticeable effect on the initial portion of the force–compression curve.

Fig. 2 shows the sensitivity of the vertical force–compression curve to variations of the hyperelastic model parameters. For reference, the experimental curve is also shown. The simulation curves pertain to a hypothetical sample with a homogeneous density equal to the volume-average density of the heterogeneous physical sample, and were generated from element simulations so that the specimen deformation remained homogeneous throughout. Thus, one would not expect these curves to coincide with the experimental curve, which pertains to an inhomogeneous physical sample. As expected, the hypothetical homogeneous samples generally exhibited higher strengths than the actual sample. Also, the shear-band bifurcation points (Rudnicki and Rice, 1975) for the homogeneously deforming samples, denoted by open dots, occurred well above the peak strength of the actual sample, suggesting the important role that heterogeneity plays in enhancing strain localization. All of the simulations showed that the bifurcation points occurred on the rising part of the load–compression curves, due in part to geometric nonlinearity that is known to enhance strain localization. We see that the initial portions of the simulation curves are nearly unaffected by the variations in κ and p_0, especially by p_0 which shows no noticeable effect on the force–compression curve. On the other hand, the elastic shear modulus μ_0 has the greatest effect on the force–compression curve. To match the initial slope of the experimental curve, we selected a base value of $\mu_0 = 30$ MPa for the shear modulus.

The parameters M and N listed in Table 2 were taken from similar sands (Jefferies, 1993), based on the median grain size and the fraction passing the No. 200 sieve on the grain size distribution curve. There has been much debate on the inherent uniqueness of the CSL (Mooney et al., 1998; Finno and Rechenmacher, 2003; Einav, 2007), and we opt not to dwell on it here. However, we note that M pertains to the slope of the CSL and not to its position on the p,q-plane (which is established by v_{c0}). The value of ρ listed in Table 2 is the limiting ellipticity before the yield surface becomes nonconvex. Ideally, the ellipticity would have been inferred from the out-of-plane normal stress σ'_2 in a plane strain test, which measures the impact of the third stress invariant, but because the specimen did not deform homogeneously we could not infer the ellipticity from the out-of-plane force data. The ellipticity value shown in Table 2 is the closest we could get despite the uncertainties in the value of the intermediate principal stress σ'_2.

Fig. 3 shows how M, N, and ρ influence the vertical force–compression curve. Higher values of M yield higher peak strengths, as expected. As for N, lower values produce higher peak strengths. The effect of the ellipticity is striking in that it magnifies the effect of the third stress invariant in plane strain compression tests. Note once again that the numerical simulation curves pertain to homogeneously deforming specimens with uniform density, so they tend to overshoot the experimental curve for the most part.

The last set of material parameters shown in Table 2 includes the hardening parameter h, plastic compressibility λ, reference specific volume, v_{c0}, and maximum plastic dilatancy parameter α. As shown in Fig. 4, none of these parameters

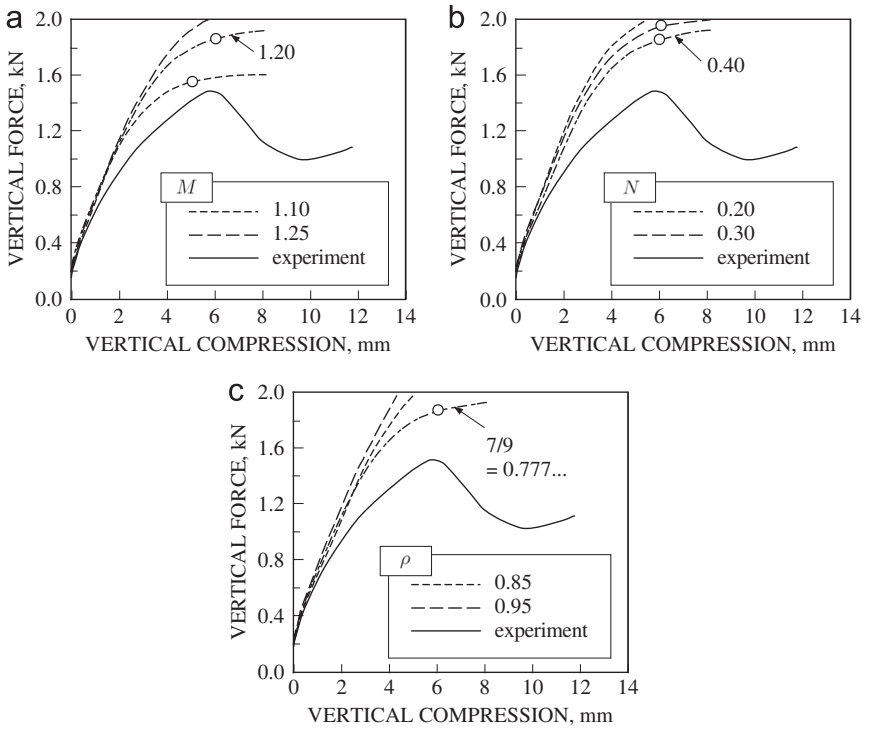

Fig. 3. Sensitivity of vertical force–vertical compression curve to shape of the yield surface: (a) slope of critical state line M; (b) exponent parameter N; and (c) ellipticity ρ. Open dots denote shear-band bifurcation points.

has any significant influence on the initial portion of the vertical force–compression curve. The hardening parameter h is not the same as the plastic modulus, i.e., softening is possible even with $h > 0$. Of these remaining parameters, α has the most significant effect on the persistent shear band as discussed in the next section. This parameter was previously thought to have a 'standard' value for most sands (Jefferies, 1993), but this is not true for the heterogeneous sand considered.

5. Shear band analysis

We consider six finite element meshes for simulating the plane strain test on the inhomogeneous sample as a boundary-value problem. The meshes are shown in Fig. 5 and include three lower resolution meshes and three higher resolution meshes. We consider two cross-diagonal patterns, one each for the coarse and fine discretizations. The rest have bias in each direction of the shear band. Each finite element is assigned a value of specific volume consistent with the results from the digitally processed CT scans. To do this, each rectangular cell is assigned a value of specific volume consistent with the averaged "CT number" over that cell. We then subdivided this cell into two triangular finite elements with the same value of specific volume. Because density is a continuum variable, mesh refinement entails refinement of the averaged CT number for each cell. In principle, we can continue refining the mesh, but because the specimen is made up of sand grains, it would not be meaningful to refine the mesh to the dimension of the grains.

The spatial variation of specific volume is shown in Fig. 6. Note from the CT image the thin dark strips appearing on the left and right vertical faces of the image. This is a transition zone that becomes more prominent as the scan approaches the faces of the specimen. This is because the specimen corners are rounded, and so they tend to project an image of a "loose" sand (darker region is higher specific volume). These thin strips also manifest themselves in the higher resolution meshes, but not in the lower resolution meshes where the elements are large enough to smear these details. In general, these details have very little effect on the ensuing shear band.

Fig. 7 shows the shear band in the specimen at a vertical compression of 8.14 mm. Superimposed on the image is the incremental displacement field calculated by Digital Image Correlation (DIC) from snapshots of the displacement fields recorded at 8.00 and 8.14 mm vertical compression. In general, there was not much variation in the shear band geometry throughout the thickness of the sample, i.e., the shear bands on the back and front faces of the soil sample were essentially the same, suggesting that the plane strain assumption was sufficient for this problem. The orientation of the shear band shown in Fig. 7 produces a left lateral downward movement of the top portion of the sample relative to the bottom portion. This movement cannot be predicted from a visual inspection of the specific volume distribution alone (see Fig. 6a).

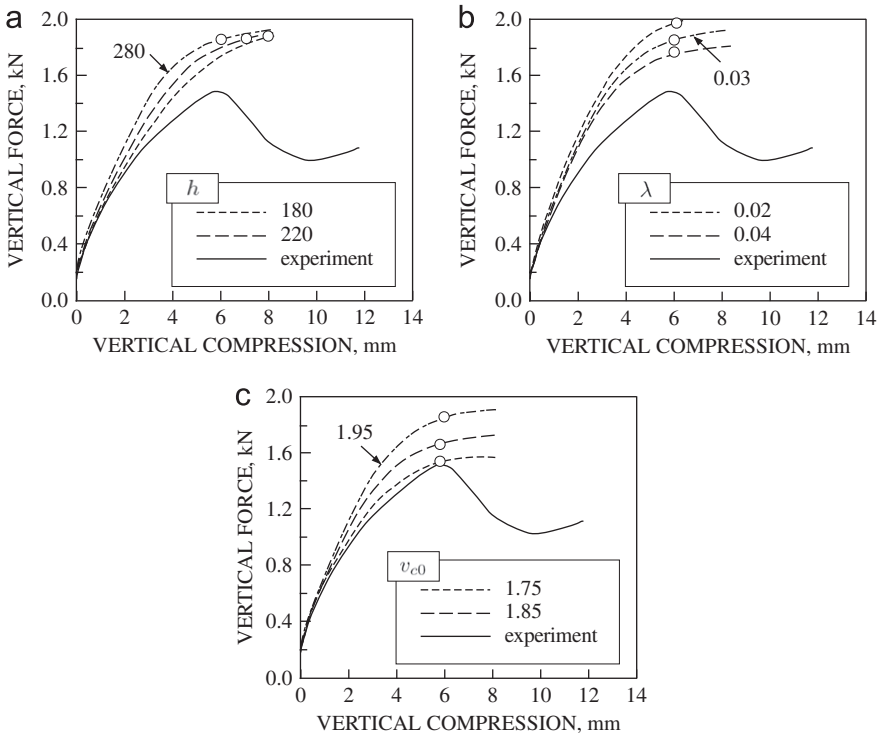

Fig. 4. Sensitivity of vertical force–vertical compression curve to hardening of the yield surface: (a) hardening parameter h; (b) plastic compressibility parameter λ; and (c) reference specific volume v_{c0} defining the position of critical state line. Open dots denote shear-band bifurcation points.

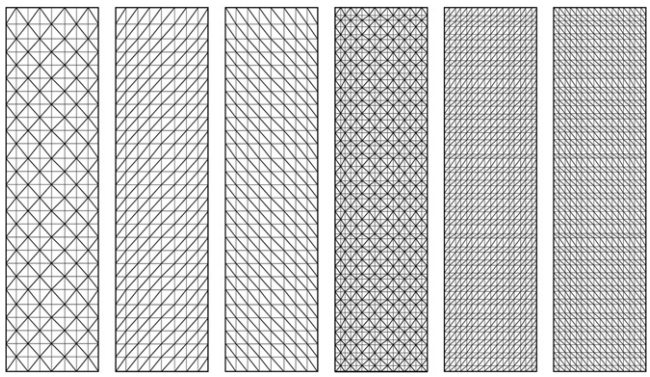

Fig. 5. Finite element meshes with constant strain triangles (CST). The lower resolution meshes have 252 nodes and 432 CST elements; the higher resolution meshes have 952 nodes and 1760 CST elements.

Fig. 8 compares the experimentally determined vertical force–vertical compression curve with the numerically generated specimen responses. The experimental curve exhibits a softening response at a nominal vertical compression of 5.5 mm. Fig. 9 shows that at this point in the test the movement of the bottom sled accelerated markedly until it leveled off at a vertical compression of around 8.9 mm due to inadvertent impedance in base sled movement caused by interference from a transducer mount. The specimen then appears to regain strength amidst acting against the impeded base. Clearly, the development of the shear band is linked to the ability of the bottom part of the sample to move in the lateral direction.

Results from the numerical simulations using the lower and higher resolution meshes, as well as from the homogeneous specimen simulation, are also shown in Fig. 8. We recall that the material parameters have been chosen so that the model follows the initial portion of the experimental load–compression curve. However, it is not possible to control the bifurcation points, so the calculated maximum loads are 'truly predicted' ultimate loads. As expected, the figure shows that the higher resolution mesh predicted a slightly softer response than the lower resolution mesh. Also as expected, the higher resolution mesh detected the onset of bifurcation (i.e., first element to satisfy the localization

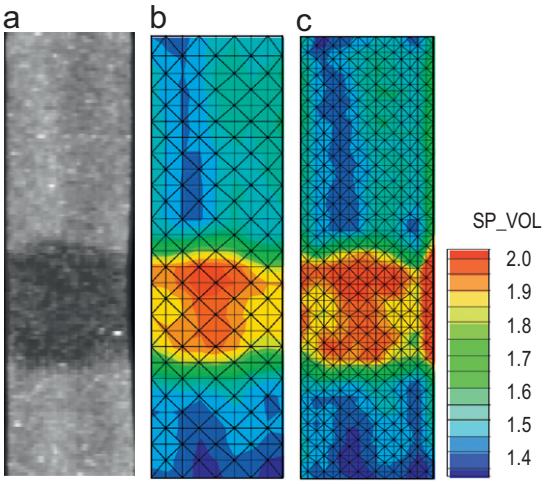

Fig. 6. Spatial variation of specific volume in the sand specimen: (a) CT image; (b) lower resolution mesh; and (c) higher resolution mesh. Color bar is specific volume. Note the wide range of values for the specific volume in the specimen (around 0.6). (For interpretation of the references to color in this figure caption, the reader is referred to the web version of this article.)

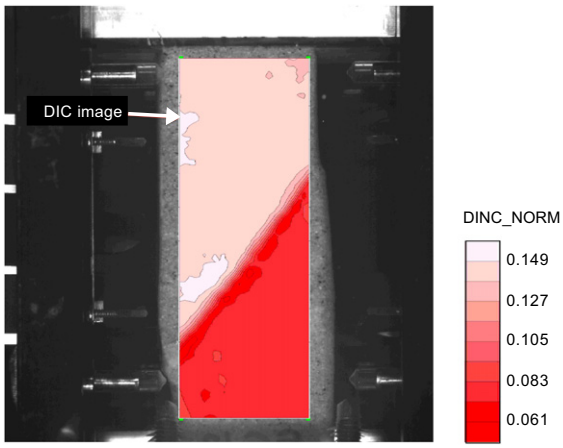

Fig. 7. Contour of norm of incremental displacement ($=\sqrt{u^2+v^2}$) from Digital Image Correlation (DIC) calculated from difference in displacement fields at 8.00 and 8.14 mm vertical compression. Color bar in mm. (For interpretation of the references to color in this figure caption, the reader is referred to the web version of this article.)

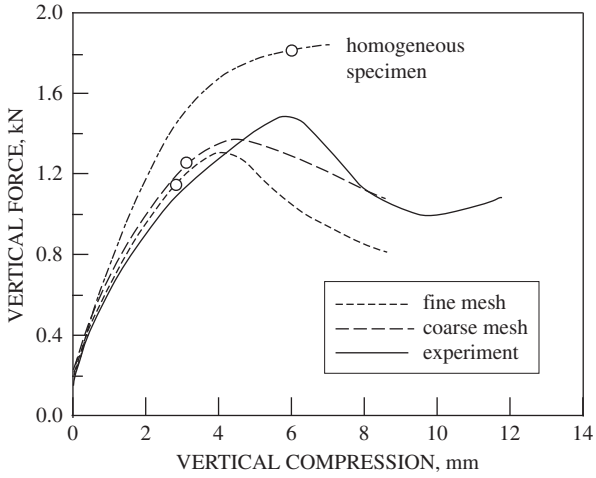

Fig. 8. Resultant force versus compression curves from plane strain experiment and numerical simulations. Open dots denote initial bifurcation points.

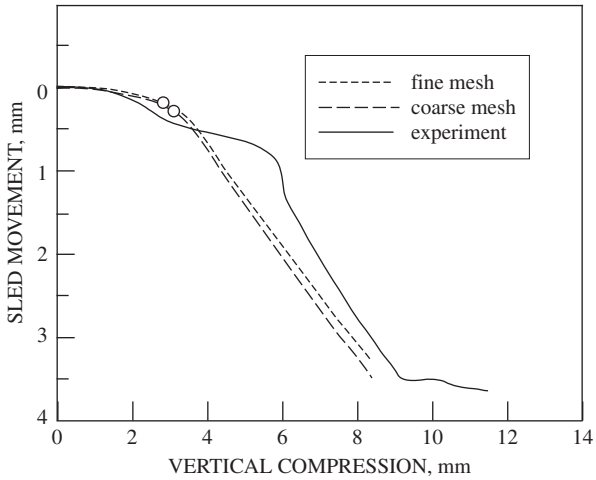

Fig. 9. Horizontal sled movement versus vertical compression from plane strain experiment and numerical simulations. Open dots denote initial bifurcation points.

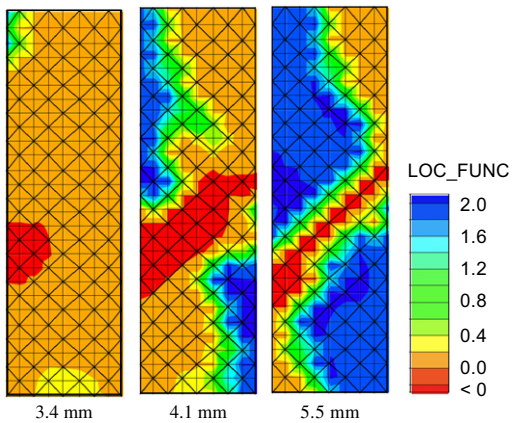

Fig. 10. Development of shear band at different stages of loading: lower resolution mesh. Numbers in mm are vertical compression of the sample. Color bar is normalized localization function, with red denoting localization. (For interpretation of the references to color in this figure caption, the reader is referred to the web version of this article.)

condition) a little bit earlier than the lower resolution mesh. The 'homogeneous' specimen simulation detected shear-band bifurcation at a much later stage of loading.

An interesting aspect of the simulations is that the load–compression curves continue to rise even after some of the elements have already satisfied the localization condition. In general, softening occurs sooner where bifurcation occurs earlier. The heterogeneous specimen simulations predicted slightly lower peak strengths, which is consistent with the movement of the bottom boundary of the specimen increasing earlier (Fig. 9). In principle, the numerical solution becomes mesh-dependent at post-bifurcation, and indeed mesh-dependent results can be seen from Fig. 8 after around 3% nominal vertical strain. For this reason, caution must be exercised in interpreting results of the analysis beyond this deformation level.

Figs. 10 and 11 show the development of a shear band in the heterogeneous soil using the coarser and finer resolution meshes, respectively. The two simulations yielded essentially similar shear bands in that the localization function, defined in Eulerian space from Eq. (12) as $F = \det(\boldsymbol{a})$, first vanishes on the left vertical face of the sample within the region of the loose sand, and then the band propagated vertically upward and to the right. As the specimen is compressed further, the contrast in the values of the localization function inside and outside the shear band becomes more pronounced. The higher resolution simulation (Fig. 11) demonstrates a more interesting pattern of shear band development not captured by the lower resolution simulation: at a vertical compression of approximately 3.4 mm, two competing shear bands emerged, each one forming in the conjugate direction of the other. The two bands merged at a vertical compression of approximately 4.1 mm, after which a persistent shear band having the same orientation as the experimentally observed shear band (Fig. 7) eventually prevailed.

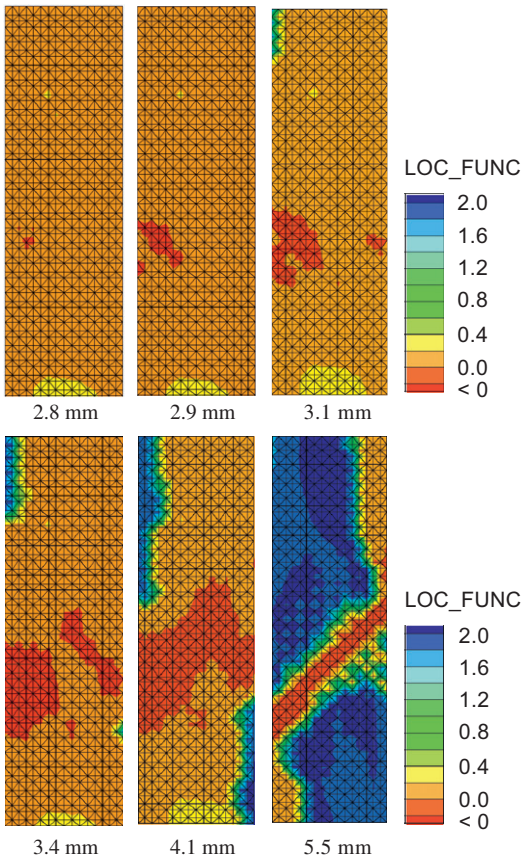

Fig. 11. Development of shear band at different values of vertical compression: higher resolution mesh. Numbers in mm are vertical compression of the sample. Color bar is normalized localization function, with red denoting localization. (For interpretation of the references to color in this figure caption, the reader is referred to the web version of this article.)

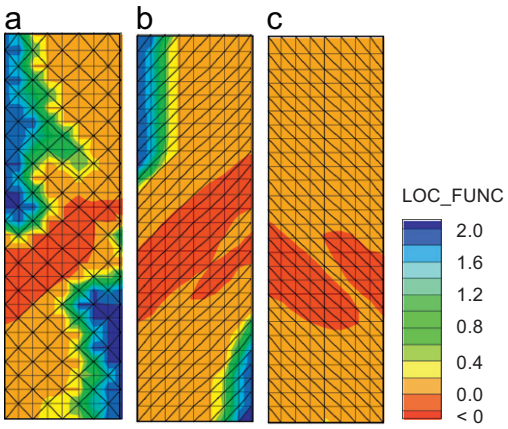

Fig. 12. Contours of normalized localization function for three lower resolution meshes at a vertical compression of 4.1 mm: (a) unbiased mesh; (b) and (c) biased meshes. Color bar is normalized localization function, with red denoting localization. (For interpretation of the references to color in this figure caption, the reader is referred to the web version of this article.)

So far we have used finite element meshes with a cross-diagonal pattern. Because of their symmetric structure, these meshes are expected to be objective with respect to the eventual shear band. Some triangular element patterns, however, tend to exhibit bias in the sense that they favor the development of one shear band over the other. These meshes have a diagonal pattern as shown in Figs. 12 and 13. The meshes with a diagonal pattern favoring the development of the 'true' shear band have no problem developing this band (Figs. 12b and 13b). However, the meshes favoring the development of

the conjugate shear band have difficulty resolving this band (Figs. 12c and 13c). In fact, with the finer resolution mesh (Fig. 13c) the 'true' shear band eventually prevailed despite the bias inherent in the mesh. This demonstrates that the shear band predicted by the mechanical model is the true shear band and is not an artifact of the numerical solution.

Dilatancy is an important element of shear band modeling since it induces a softening response particularly in geomaterials (Tejchman and Wu, 2010). The constitutive model prescribes a maximum limit to dilatancy of a geomaterial, represented by D^* in Eq. (25) through the material parameter α. The latter is normally taken to have a "constant" value of $\alpha \approx -3.5$ (Jefferies, 1993), but in the present specimen simulations where the specific volume varies by a wide range, we find this value of α to produce unreasonable results. Fig. 14 shows deformed low-resolution meshes after applying a vertical compression of 5.5 mm. We see that the more negative values of α produced higher dilatancy in the initially loose soil region after vertical compaction. This may be traced from the fact that most shearing occurred in this more compressible region, causing the soil to subsequently dilate after being subjected to vertical compression. The more negative values of α then resulted in local lateral bulging of the soil sample, with little propensity to develop a shear band. However, values of α in the range $[-0.5, -1.5]$ seem to capture the initiation of a persistent shear band.

Before closing, we note that the simulations in this paper did not include any finite element enhancement arising from the appearance of a shear band, such as that provided by the assumed enhanced strain or extended finite element methods (Borja, 2000, 2008; Borja and Regueiro, 2001). Whereas post-localization simulations are commonplace for materials with homogeneous properties, the presence of inhomogeneities renders these techniques less straightforward to use. In the first place, sands do have a tendency to develop a complicated pattern of shear bands because of their particulate nature. What may seem like a nucleating shear band may stop from developing to allow another band to grow somewhere else. This is evident from Fig. 11, which shows a shear band that appeared to nucleate after applying a vertical compression

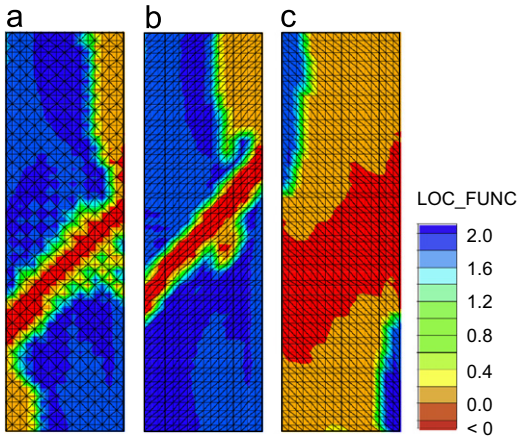

Fig. 13. Contours of normalized localization function for three higher resolution meshes at a vertical compression of 5.5 mm: (a) unbiased mesh; (b) and (c) biased meshes. Color bar is normalized localization function, with red denoting localization. (For interpretation of the references to color in this figure caption, the reader is referred to the web version of this article.)

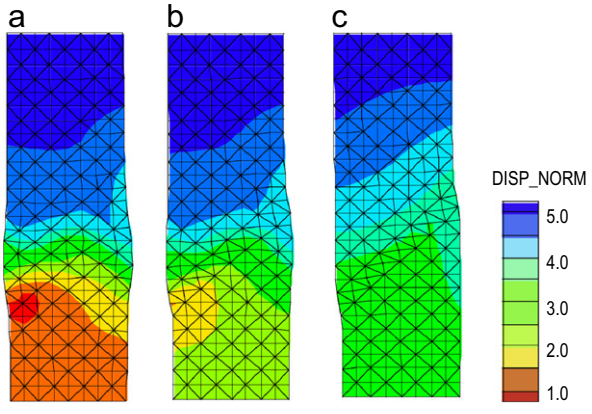

Fig. 14. Deformed meshes (no magnification) after applying a vertical compression of 5.5 mm: (a) $\alpha = -3.5$; (b) $\alpha = -2.5$; and (c) $\alpha \in [-1.5, -0.5]$. Note that the less negative values of α trigger a shear band mode, whereas the more negative values simply induce local lateral bulging. Color bar is norm of total displacement field in mm. (For interpretation of the references to color in this figure caption, the reader is referred to the web version of this article.)

of 2.1 mm (red region). This same point regained stability at a later stage in the solution, and is not even included in the domain of the final shear band. Essentially, this initial point of localization is nothing but noise.

If we enhanced the initial point of localization, we would have to introduce a slip weakening law into the system to allow the response to transition into the post-localization regime (Borja and Foster, 2007). We would also have to enhance the band to propagate in the conjugate direction as implied by the orientation of the partially developing band at a vertical compression of around 2.9 mm. Clearly, this would lead to the prediction of an incorrect shear band. The question, of course, is whether the predicted shear band is indeed the correct one, given that the solution was not enhanced to circumvent potential mesh-dependency issues. The answer can be gleaned from Fig. 8, which shows that mesh-dependency between the coarser and finer mesh solutions appears to manifest itself only at post-peak when both meshes had already identified the same persistent shear band. Once the persistent shear band has been identified, it is a relatively straightforward matter to embed a post-localization enhancement into the finite element solution (Borja and Regueiro, 2001; Regueiro and Borja, 2001; Borja, 2000).

6. Conclusions

Spatial density variation is a determining factor for the development of a persistent shear band in a symmetrically loaded sand body. Depending on density contrast, the true shear band can be resolved even with a biased finite element mesh, such as a mesh with triangular elements having a diagonal pattern. Dilatancy is found to have a significant influence on the capture of a persistent shear band. While this is not a new conclusion, the impact of maximum dilatancy on the capture of a shear band has not been fully understood before the present work. Too much dilatancy inhibits the formation of a shear band in a sand body having a strong density contrast. These conclusions would not have been reached without today's advanced imaging technology and robust computational modeling tools, which permit a combined experimental imaging and finite element modeling of strain localization processes in granular soils.

Acknowledgments

Support for this work was provided by the US National Science Foundation (NSF) under Contract numbers CMS-0324674 and CMMI-0936421 to Stanford University and the University of Southern California, and by Fonds zur Förderung der wissenschaftlichen Forschung (FWF) of Austria under Project number L656-N22 to Universität für Bodenkultur. We wish to thank Professor K. Bhattacharya and two anonymous reviewers for reviewing our work.

References

Alshibli, K.A., Hasan, A., 2008. Spatial variation of void ratio and shear band thickness in sand using X-ray computed tomography. Géotechnique 58, 249–257.
Alshibli, K.A., Sture, S., Costes, N.C., Frank, M.L., Lankton, F.R., Batiste, S.N., Swanson, R.A., 2000. Assessment of localized deformations in sand using X-ray computed tomography. Geotech. Test. J. 23, 274–299.
Alshibli, K.A., Sture, S., 2000. Shear band formation in plane strain compression. J. Geotech. Geoenviron. Eng. 126, 495–503.
Alshibli, K.A., Sture, S., 1999. Sand shear band thickness measurements by digital imaging techniques. J. Comput. Civ. Eng. 13, 103–109.
Andrade, J.E., Borja, R.I., 2006. Capturing strain localization in dense sands with random density. Int. J. Numer. Methods Eng. 67, 1531–1564.
Argyris, J.H., Faust, G., Szimmat, J., Warnke, E.P., Willam, K.J., 1974. Recent developments in the finite element analysis of prestressed concrete reactor vessels. Nuclear Eng. Des. 28, 42–75.
Ashby, M.F., Hallam, S.D., 1986. The failure of brittle solids containing small cracks under compressive stress states. Acta Metall. 16, 497–510.
Borja, R.I., 2008. Assumed enhanced strain and the extended finite element methods: a unification of concepts. Comput. Methods Appl. Mech. Eng. 197, 2789–2803.
Borja, R.I., Foster, C.D., 2007. Continuum mathematical modeling of slip weakening in geological systems. J. Geophys. Res. 112 (B04301). doi:10.1029/2005JB004056.
Borja, R.I., Andrade, J.E., 2006. Critical state plasticity. part VI: meso-scale finite element simulation of strain localization in discrete granular materials. Comput. Methods Appl. Mech. Eng. 195, 5115–5140.
Borja, R.I., Sama, K.M., Sanz, P.F., 2003. On the numerical integration of three-invariant elastoplastic constitutive models. Comput. Methods Appl. Mech. Eng. 192, 1227–1258.
Borja, R.I., 2002. Bifurcation of elastoplastic solids to shear band mode at finite strain. Comput. Methods Appl. Mech. Eng. 191, 5287–5314.
Borja, R.I., Regueiro, R.A., 2001. Strain localization of frictional materials exhibiting displacement jumps. Comput. Methods Appl. Mech. Eng. 190, 2555–2580.
Borja, R.I., 2000. A finite element model for strain localization analysis of strongly discontinuous fields based on standard Galerkin approximation. Comput. Methods Appl. Mech. Eng. 190, 1529–1549.
Borja, R.I., Tamagnini, C., 1998. Cam-Clay plasticity, Part III: extension of the infinitesimal model to include finite strains. Comput. Methods Appl. Mech. Eng. 155, 73–95.
Borja, R.I., Tamagnini, C., Amorosi, A., 1997. Coupling plasticity and energy-conserving elasticity models for clays. J. Geotech. Geoenviron. Eng. ASCE 123, 948–957.
Borja, R.I., 1991. Cam-Clay plasticity, Part II: implicit integration of constitutive equation based on a nonlinear elastic stress predictor. Comput. Methods Appl. Mech. Eng. 88, 225–240.
Borja, R.I., Lee, S.R., 1990. Cam-Clay plasticity, Part I: implicit integration of elasto-plastic constitutive relations. Comput. Methods Appl. Mech. Eng. 78, 49–72.
Bruck, H.A., McNeill, S.R., Sutton, M.A., Peters III, W.H., 1989. Digital image correlation using Newton–Raphson method of partial differential corrections. Exp. Mech. 29, 261–268.
Chen, W.F., Han, D.J., 1988. Plasticity for Structural Engineers. Springer-Verlag, Berlin, Germany.

Chupin, O., Rechenmacher, A.L., Abedi, S., 2011. Finite strain analysis of nonuniform deformations inside shear bands in sands. Int. J. Numer. Anal. Methods Geomech., doi:10.1002/nag.1071.
Coumoulos, D.G., 1968. A Radiographic Study of Soils. Ph.D. Thesis. Cambridge University, Cambridge, UK.
Desrues, J., 1984. La Localisation de la Deformation dans les Materiaux Granulaires. These de Doctorat es Science, Universite Scientifique et Medicale de Grenoble, France.
Desrues, J., Lanier, J., Stutz, P., 1985. Localization of the deformation in tests on sand sample. Eng. Fract. Mech. 21, 909–921.
Desrues, J., Chambon, R., Mokni, M., Mazerolle, F., 1996. Void ratio evolution Inside shear bands in triaxial sand specimens studied by computed tomography. Géotechnique 46, 529–546.
Einav, I., 2007. Soil mechanics: breaking ground. Philos. Trans. R. Soc. A 365, 2985–3002.
Evans, T.M., Frost, J.D., 2010. Multiscale investigation of shear bands in sand: physical and numerical experiments. Int. J. Numer. Anal. Methods Geomech. 34, 1634–1650.
Finno, R.J., Rechenmacher, A.L., 2003. Effect of consolidation history on critical state of sand. J. Geotech. Eng. 129, 350–360.
Gudehus, G., 1973. Elastoplastische stoffgleichungen für trockenen sand. Ing. Arch. 42, 151–169.
Harris, W.W., Viggiani, G., Mooney, M.A., Finno, R.J., 1995. Use of stereophotogrammetry to analyze the development of shear bands in sand. Geotech. Test. J. 18, 405–420.
Hasan, A., Alshibli, K.A., 2010. Experimental assessment of 3D particle-to-particle interaction within sheared sand using synchrotron microtomography. Géotechnique 60, 369–379.
Holtz, R.D., 1991. Stress distribution and settlement of shallow foundations. In: Fang, H.-Y. (Ed.), Foundation Engineering Handbook2nd ed . VanNostrand Reinhold, New York.
Horii, H., Nemat-Nasser, S., 1985. Compression-induced micro-crack growth in brittle solids: axial splitting and shear failure. J. Geophys. Res. 90, 3105–3215.
Jang, D.J., Frost, J.D., 2000. Use of image analysis to study the microstructure of a failed sand specimen. Can. Geotech. J. 37, 1141–1149.
Jefferies, M.G., 1993. Nor-sand: a simple critical state model for sand. Géotechnique 43, 91–103.
Jiang, J., Pietruszczak, 1988. Convexity of yield loci for pressure sensitive materials. Comput. Geotech. 5, 51–63.
Kolymbas, D., 2009. Kinematics of shear bands. Acta Geotech. 4, 315–318.
Kulhawy, F.H., Mayne, P.W., 1990. Manual on Estimating Soil Properties for Foundation Design. Report EL-6800. Electric Power Research Institute, Palo Alto, August.
Liang, L., Saada, A., Figueroa, J.L., Cope, C.T., 1997. The use of digital image processing in monitoring shear band development. Geotech. Test. J. 20, 324–339.
Matsushima, T., Ishii, T., Konagai, K., 2002. Observation of grain motion in the interior of a PSC test specimen by laser-aided Tomography. Soils Found. 42, 27–36.
Mooney, M.A., Finno, R.J., Viggiani, G., Harris, W.W., 1996. Issues of uncertainty regarding localized strains in granular soils. In: Proceedings Uncertainty '96, vol. 1, ASCE, Reston, VA, pp. 312–325.
Mooney, M.A., Finno, R.J., Viggiani, G., 1998. A unique critical state for a sand? J. Geotech. Geoenviron. Eng. 124, 1100–1108.
Oda, M., Kazama, H., 1998. Microstructure of shear bands and its relation to the mechanisms of dilatancy and failure of dense granular soils. Géotechnique 48, 465–481.
Poulos, H.G., 1975. Settlement of isolated foundations. In: Valliappan, S., Hain, S., Lee, I.K. (Eds.), Soil Mechanics—Recent Developments. William H Sellen Pty., Zetland, pp. 181–212.
Read, H.E., Hegemier, G.A., 1984. Strain softening of rock, soil and concrete—a review article. Mech. Mater. 3, 271–294.
Rechenmacher, A.L., Abedi, S., Chupin, O., Orlando, A.D., 2011. Characterization of mesoscale instabilities in localized granular shear using digital image correlation. Acta Geotech. 6, 205–217.
Rechenmacher, A.L., Chupin, O., Abedi, S., 2010. Evolution of force chains in shear bands in sands. Géotechnique 60, 343–351.
Rechenmacher, A.L., 2006. Grain-scale processes governing shear band initiation and evolution in sands. J. Mech. Phys. Solids 54, 22–45.
Rechenmacher, A.L., Finno, R.J., 2004. Digital image correlation to evaluate shear banding in dilative sands. Geotech. Test. J. 27, 13–22.
Regueiro, R.A., Borja, R.I., 2001. Plane strain finite element analysis of pressure-sensitive plasticity with strong discontinuity. Int. J. Solids Struct. 38, 3647–3672.
Rice, J.R., Rudnicki, J.W., 1980. A note on some features of the theory of localization of deformation. Int. J. Solids Struct. 16, 597–605.
Roscoe, K.H., Burland, J.B., 1969. On the generalized stress-strain behavior of 'wet' clay. In: Heyman, J., Leckie, F.A. (Eds.), Engineering Plasticity. Cambridge Univ. Press, Cambridge, pp. 535–609.
Rudnicki, J.W., Rice, J.R., 1975. Conditions for the localization of deformation in pressure sensitive dilatant materials. J. Mech. Phys. Solids 23, 371–394.
Sfriso, A., Weber, G., 2010. Formulation and validation of a constitutive model for sands in monotonic shear. Acta Geotech. 5, 257–272.
Shapiro, S., Yamamuro, J.A., 2003. Effects of silt on three-dimensional stress–strain behavior of loose sand. J. Geotech. Geoenviron. Eng. 129, 1–11.
Stroud, M.A., 1971. The Behavior of Sand at Low Stress Levels in the Simple Shear Apparatus. Ph.D. Thesis. University of Cambridge, Cambridge, UK.
Sutton, M.A., McNeill, S.R., Helm, J.D., Chao, Y.J., 2000. Advances in two-dimensional and three-dimensional computer vision. Photomech. Top. Appl. Phys. 77, 323–372.
Tagliaferri, F., Waller, J., Andó, E., Hall, S.A., Viggiani, G., Bésuelle, P., DeJong, J.T., 2011. Observing strain localization processes in bio-cemented sand using X-ray imaging. Granular Matter 13, 247–250.
Tejchman, J., Wu, W., 2010. Non-coaxiality and stress-dilatancy rule in granular materials: FE investigation within micro-polar hypoplasticity. Int. J. Numer. Anal. Methods Geomech. 33, 117–142.
Tejchman, J., Bauer, E., Tantono, S.F., 2007. Influence of initial density of cohesionless soil on evolution of passive earth pressure. Acta Geotech. 2, 53–63.
Vesic, A.S., 1975. Bearing capacity of shallow foundations. In: Winterkorn, H., Fang, H.Y. (Eds.), Foundation Engineering Handbook. Van Nostrand Reinhold, New York.
Viggiani, G., Finno, R.J., Harris, W.W., 1994. Experimental observations of strain localisation in plane strain compression of a stiff clay. In: Chambón, R., Desrues, J., Vardoulakis, I. (Eds.), Localization and Bifurcation Theory for Soils and Rocks. Balkema, Rotterdam, The Netherlands, pp. 189–198.
Wellington, S.L., Vinegar, H.J., 1987. X-ray computerized tomography. J. Pet. Geol. 39, 885–898.
Willam, K.J., Warnke, E.P., 1974. Constitutive Model for Triaxial Behavior of Concrete. Concrete Structures Subjected to Triaxial Stresses, International Association for Bridges and Structural Engineering, Bergamo, Italy.
Yoshida, T., Tatsuoka, F., Kamegai, Y., Siddiquee, M.S.A., Park, C.S., 1994. Shear banding in sands observed in plane strain compression. In: Proceedings of the Third International Workshop on Localisation and Bifurcation Theory for Soils and Rocks, Aussois, France, Rotterdam, Balkema, pp. 165–179.